ACS NANO
Cite This: ACS Nano 2019, 13, 10929−10938
www.acsnano.org

ARTICLE

Epitaxial Synthesis of Monolayer $PtSe_2$ Single Crystal on $MoSe_2$ with Strong Interlayer Coupling

Jiadong Zhou,[†,●] Xianghua Kong,[‡,§,●] M. Chandra Sekhar,[∥,⊥,●] Junhao Lin,[*,#] Frederic Le Goualher,[†] Rui Xu,[§,▽] Xiaowei Wang,[†] Yu Chen,[○] Yao Zhou,[○] Chao Zhu,[†] Wei Lu,[∥,⊥] Fucai Liu,[†] Bijun Tang,[†] Zenglong Guo,[#] Chao Zhu,[†] Zhihai Cheng,[§,▽] Ting Yu,[○] Kazu Suenaga,[◆] Dong Sun,[*,∥,⊥] Wei Ji,[*,§] and Zheng Liu[*,†,¶]

[†]School of Materials Science and Engineering, Nanyang Technological University, 639798 Singapore
[‡]Department of Physics and Centre for the Physics of Materials, McGill University, Montreal, Quebec H3A 2T8, Canada
[§]Department of Physics and Beijing Key Laboratory of Optoelectronic Functional Materials and Micro-nano Devices, Renmin University of China, Beijing 100872, China
[∥]International Center for Quantum Materials, School of Physics, Peking University, Beijing 100871, China
[⊥]Collaborative Innovation Center of Quantum Matter, Beijing 100871, China
[#]Department of Physics, Southern University of Science and Technology, Shenzhen 518055, China
[▽]CAS Key Laboratory of Standardization and Measurement for Nanotechnology, CAS Center for Excellence in Nanoscience, National Center for Nanoscience and Technology, Beijing 100190, China
[○]Centre for Disruptive Photonic Technologies, School of Physical and Mathematical Sciences, Nanyang Technological University, 637371 Singapore
[◆]National Institute of Advanced Industrial Science and Technology (AIST), Tsukuba 305-8565, Japan
[¶]CNRS International NTU THALES Research Alliances, UMI 3288, Research Techno Plaza, 50 Nanyang Drive, Border X Block, Level 6, 637553 Singapore

Supporting Information

ABSTRACT: **$PtSe_2$, a layered two-dimensional transition-metal dichalcogenide (TMD), has drawn intensive attention owing to its layer-dependent band structure, high air stability, and spin-layer locking effect which can be used in various applications for next-generation optoelectronic and electronic devices or catalysis applications. However, synthesis of $PtSe_2$ is highly challenging due to the low chemical reactivity of Pt sources. Here, we report the chemical vapor deposition of monolayer $PtSe_2$ single crystals on $MoSe_2$. The periodic Moiré patterns from the vertically stacked heterostructure ($PtSe_2/MoSe_2$) are clearly identified *via* annular dark-field scanning transmission electron microscopy. First-principles calculations show a type II band alignment and reveal interface states originating from the strong−weak interlayer coupling (SWIC) between $PtSe_2$ and $MoSe_2$ monolayers, which is supported by the electrostatic force microscopy imaging. Ultrafast hole transfer between $PtSe_2$ and $MoSe_2$ monolayers is observed in the $PtSe_2/MoSe_2$ heterostructure, matching well with the theoretical results. Our study will shed light on the synthesis of Pt-based TMD heterostructures and boost the realization of SWIC-based optoelectronic devices.**

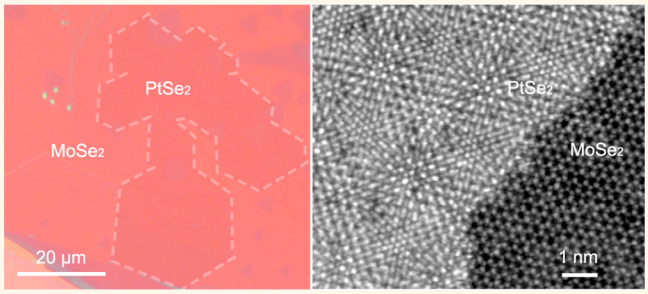

KEYWORDS: *$PtSe_2$, $PtSe_2/MoSe_2$ heterostructure, two-dimensional material, chemical vapor deposition, interlayer coupling*

Platinum diselenide ($PtSe_2$) is an intriguing layered material due to its helical spin texture induced by local Rashba effect[1] and strong interlayer coupling.[2,3] Recent work also revealed that the strong interlayer coupling can

Received: December 15, 2018
Accepted: September 24, 2019
Published: September 24, 2019

DOI: 10.1021/acsnano.8b09479
ACS Nano 2019, 13, 10929−10938

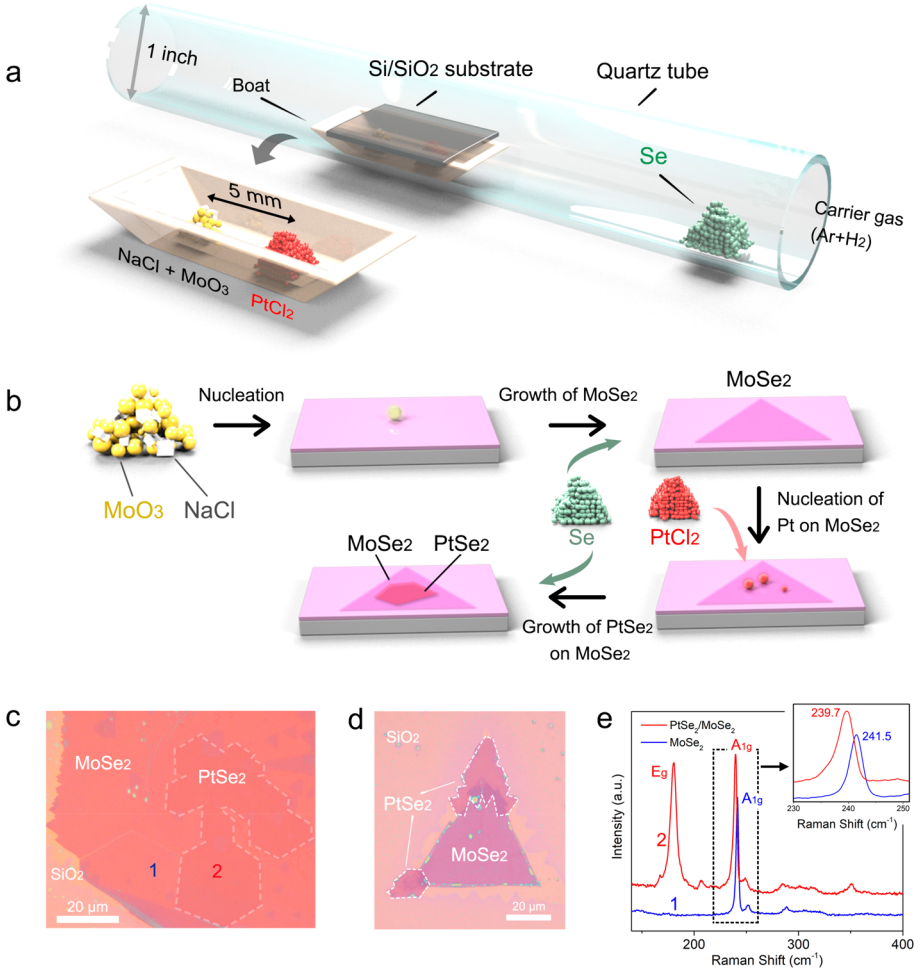

Figure 1. Reaction system and spectroscopy characterizations of $PtSe_2/MoSe_2$ vertical heterostructures. (a) Reaction system used to synthesize $PtSe_2$ and $PtSe_2/MoSe_2$ vertical heterostructure and the atomic crystal structure of $PtSe_2/MoSe_2$. (b) Growth mechanism of $PtSe_2/MoSe_2$ heterostructure. (c and d) Optical images of as-synthesized $PtSe_2/MoSe_2$ heterostructure with different styles. From the optical images, the size of the overlapped vertical heterostructure is about 40 μm, and the area of the vertical heterostructure is larger than 1000 μm^2. (e) The Raman spectra in the positions 1 and 2 of the heterostructure (inset shows the optical image of the vertical heterostructure). The A_{1g} mode located at 240 cm^{-1} confirms that the crystal is $MoSe_2$. The Raman peaks located at 175 and 205 cm^{-1} originate from the E_g mode of $PtSe_2$. The Raman peaks located at 240 cm^{-1} can be contributed to the A_{1g} vibration mode of $MoSe_2$. These indicate that the as-synthesized $PtSe_2$ and $MoSe_2$ form the vertical heterostructure. Notably, the A_{1g} mode of $MoSe_2$ from the $PtSe_2/MoSe_2$ heterostructure shows a little shift due to the coupling between $PtSe_2$ and $MoSe_2$.

induce a $PtSe_2$ transition from a semimetal (bulk) to a semiconductor (monolayer) with a band gap increasing from 0 to 1.2 eV.[4,5] The narrow bandgap of few layer $PtSe_2$ renders it an excellent candidate for broadband mid-infrared detectors.[3,6,7] Furthermore, field-effect transistors (FETs) based on few-layer $PtSe_2$ display high mobility and good stability in air.[5] All these fascinating results indicate that $PtSe_2$ can be an attractive candidate for various applications in electronic and optoelectronic devices.[8] Therefore, controlled synthesis of high-quality and atomically thin $PtSe_2$ layers is urgently required. So far, the mechanical exfoliation has been widely adopted to produce $PtSe_2$ monolayers. However, this method is low yield and time-consuming and usually leads to small size $PtSe_2$ flakes. Although few-layered $PtSe_2$ can be synthesized by selenization of Pt films or molecular beam epitaxy (MBE),[9−12] synthesis of large size monolayer $PtSe_2$ single crystals is yet to be achieved, due to the low chemical reactivity of Pt.[1,2,12,13]

Here, we demonstrate the synthesis of monolayer $PtSe_2$ using the chemical vapor deposition (CVD) method. Various substrates including SiO_2/Si, Al_2O_3, and $MoSe_2$ have been used for the growth of $PtSe_2$. It is found that $PtSe_2$ monolayers can only be epitaxially grown on $MoSe_2$ substrate, forming a $PtSe_2/MoSe_2$ vertical heterostructure. Such structure is confirmed by the Moiré fringe from annular dark-field scanning transmission electron microscopy (ADF-STEM). First-principles calculations show that the formed heterostructure has a direct band gap and forms a type II band alignment. A more striking result lies in the emergence of interface states located within the original bandgap. These states are hybridized by the wave functions of Se-p_z and Pt/Mo-d_{z^2} orbitals from the $PtSe_2$ monolayer and $MoSe_2$ monolayer whose intrinsic interlayer couplings are strong and weak, respectively, in their own multilayers. The edge states of $PtSe_2$ on $MoSe_2$ observed with electrostatic force microscopy (EFM) compellingly support the existence of the theoretically predicted interface states. The charge transfer from $PtSe_2$ to $MoSe_2$ probed by ultrafast electron dynamics further demonstrates the interlayer coupling and band alignment in the $PtSe_2/MoSe_2$ heterostructure. Our work is helpful toward the synthesis of a $PtSe_2$ monolayer and

DOI: 10.1021/acsnano.8b09479
ACS Nano 2019, 13, 10929−10938

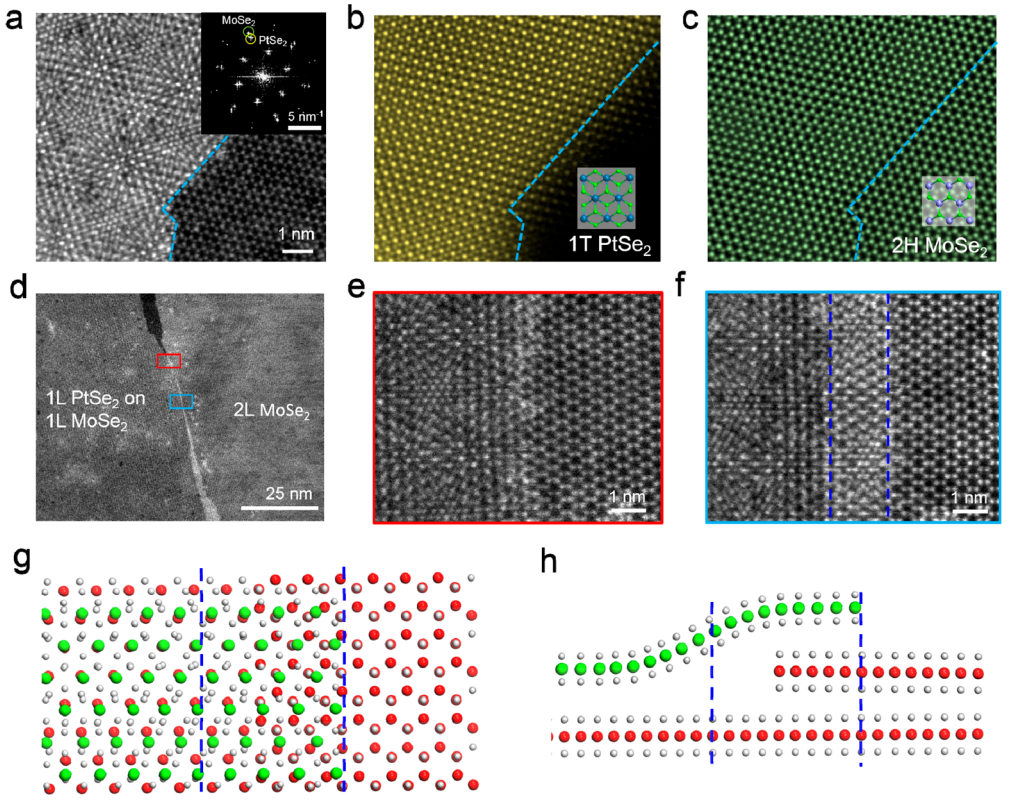

Figure 2. Atomic structure of the vertically stacked $PtSe_2/MoSe_2$ heterostructure and lateral boundary. (a) Experimental atomic-resolution ADF-STEM image of $PtSe_2/MoSe_2$, showing the periodic Moiré pattern where the monolayer $PtSe_2$ stacks on top of monolayer $MoSe_2$. Inset shows the FFT pattern obtained from (a), where the lattice constants of 0.376 and 0.332 nm correspond to the lattice of $PtSe_2$ and $MoSe_2$, as highlighted by the yellow and green circles, respectively. (b and c) Inverse FFT image of (a) by selectively filtering out the $PtSe_2$ (b) and $MoSe_2$ (c) lattice information in the FFT pattern, respectively. The 1T phase of $PtSe_2$ and 1H phase of $MoSe_2$ are confirmed by their discrete contrast which are consistent with the overlaid atomic models. (d) Low-magnification STEM image of the lateral boundary in a bilayer region. The left part is the $PtSe_2/MoSe_2$ heterostructure, while the right part is bilayer $MoSe_2$. (e and f) Atomic-resolution images of the highlighted regions in (d), showing the initial stage (e) and the overlapping region (f) of the lateral boundary. The initial stage shows a sharp change from $PtSe_2$ to $MoSe_2$ lattice with some tiny regions of bright contrast along the edge, indicating both $PtSe_2$ and $MoSe_2$ lattices have a sharp edge termination without any chemical bonding. The $PtSe_2$ and $MoSe_2$ gradually overlapped with each other along the boundary. (g and h) The top (g) and side (h) views of the schematic atomic models of the overlapping lateral boundary.

demonstrates its potential in electronic and optoelectronic devices.

RESULTS AND DISCUSSION

Herein, the epitaxial growth of $PtSe_2$ on $MoSe_2$ was achieved by using $PtCl_2$ and MoO_3/NaCl mixed powders as sources.[14] More information about the growth is provided in the Methods section. Figure 1a illustrates the reaction system for the growth of $PtSe_2$ crystals. Figure 1b shows the proposed growing mechanism. Monolayer $PtSe_2$ single crystals were obtained on a $MoSe_2$ substrate with a one-step CVD method, as shown in Figure 1c,d. Generally, most of the as-grown samples were vertically stacked $PtSe_2/MoSe_2$. We believe that the large lattice mismatch between $PtSe_2$ and $MoSe_2$ (1T for $PtSe_2$ and 1H for $MoSe_2$) hinders the epitaxial growth of $PtSe_2$ and $MoSe_2$ in-plane heterostructure. Figure 1c shows the hexagonal $PtSe_2$ monolayers atop the $MoSe_2$ monolayer with a lateral size of ~30 μm. Such size is much larger than the previously reported value.[13] Atomic force microscopy (AFM) was conducted to determine the height of the as-prepared $PtSe_2/MoSe_2$ heterostructure. The thickness of $PtSe_2$ is ~0.8 nm, confirming its monolayer nature (Figure S1). More optical images along with the size distribution of $PtSe_2$ flakes are provided in Figure S2. The second layer $MoSe_2$ which coexists with monolayer $PtSe_2$ can also be found in some synthesized samples. The area of the $PtSe_2/MoSe_2$ heterostructure (Figure 1c) can be up to ~1000 μm^2. The size comparison is shown in Figure S3.[15−22] Meanwhile, we also observed that $PtSe_2$ monolayers can grow not only epitaxially on top of $MoSe_2$ but also partially overlap with $MoSe_2$ due to the different growing rates of $PtSe_2$ and $MoSe_2$, as shown in Figure 1d. This should be attributed to the nucleation formation of $PtSe_2$ on the edge of $MoSe_2$, which then grows outward (down the step). The Raman spectrum and thickness of $PtSe_2$ with a similar morphology is shown in Figure S4.

In order to demonstrate the role of $MoSe_2$, time-dependent experiments were carried out. For a short growing time (3 min), only $MoSe_2$ can be observed. By increasing the growing time to 10 min, the $PtSe_2/MoSe_2$ heterostructure can be obtained (see Figure S5). We also used different substrates including exfoliated $MoSe_2$ flakes, SiO_2/Si, and sapphire wafers to synthesize $PtSe_2$ crystals. Only $PtSe_2$ thick flakes and particles can be obtained on exfoliated $MoSe_2$ flakes (Figure S6). For SiO_2/Si and sapphire substrates, at the growing temperature of ~400 °C, only polycrystalline $PtSe_2$ films can be obtained (Figure S7). Increasing the growing temperature to ~810 °C will result in few-layer $PtSe_2$ single crystal (Figures S8 and S9). These results are consistent with previous reports

DOI: 10.1021/acsnano.8b09479
ACS Nano 2019, 13, 10929−10938

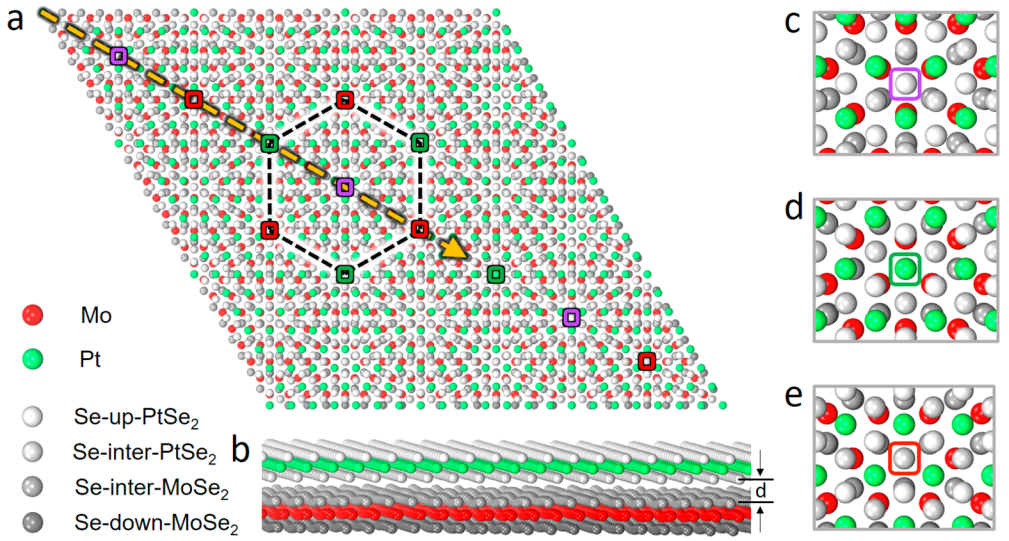

Figure 3. Geometry information on $PtSe_2$(1T)/$MoSe_2$(1H) vertical heterostructures. (a and b) Top and side views of the geometry structure of $PtSe_2$(1T)/$MoSe_2$(1H) vertical heterostructures. The violet, green, and red rectangles denote three high-symmetry stacking local configurations which have been zoomed in in (c) $Se_{inter}(PtSe_2)-Se_{inter}(MoSe_2)$ stacking, (d) $Pt-Se_{inter}(MoSe_2)$ stacking, and (e) $Se_{inter}(PtSe_2)-Mo$ stacking, respectively. And parameter *d* marked in (b) refers to the interlayer distance between $PtSe_2$(1T) and $MoSe_2$(1H).

on the growth of $PtSe_2$ flakes on MoS_2.[9,13] Based on these results, it can be concluded that the CVD-grown $MoSe_2$ monolayer is a good candidate for the epitaxial growth of $PtSe_2$ monolayer.

The successful growth of $PtSe_2$ monolayer on $MoSe_2$ can be attributed to the following two reasons: (1) The chemical reactivity between Mo precursors and Se is higher than that between Pt precursor and Se and the vapor pressure of Mo precursors is relatively higher than that of Pt precursor.[14] As a result, the growing rate of $MoSe_2$ is faster than that of $PtSe_2$, which makes $MoSe_2$ grow first. (2) The lattice mismatch between $PtSe_2$ and $MoSe_2$ is smaller than that between $PtSe_2$ and SiO_2/Si (or Al_2O_3). Therefore, $MoSe_2$ is a favorable substrate for the epitaxial growth of $PtSe_2$ monolayer (comparison is provided in Table S1). We also noticed that, at a relatively high growing temperature (~810 °C), $MoSe_2$ flakes could be etched by H_2, which will result in $MoSe_2$ flakes with different geometries.

Raman spectroscopy was carried out to investigate the structure and quality of formed $PtSe_2$/$MoSe_2$ heterostructures. Figure 1e shows the Raman spectra collected from points 1 and 2 of the sample shown in Figure 1c. The sole peak located at 240 cm^{-1} from point 1 (blue curve) corresponds to the A_{1g} mode of $MoSe_2$.[23] Raman peaks sitting at 175, 205, and 240 cm^{-1} were collected from point 2 (red curve), corresponding to the E_g and A_{1g} modes of $PtSe_2$[24] and the A_{1g} mode of $MoSe_2$, respectively. Notably, the A_{1g} mode of $MoSe_2$ in the $PtSe_2$/$MoSe_2$ heterostructure shows a red shift due to the interlayer coupling between $PtSe_2$ and $MoSe_2$, which is consistent with the experimental observations reported result[11] and theoretical results.[25] Interestingly, from point 2, a Raman peak located at ~350 cm^{-1} can be found, which could be attributed to the interlayer coupling between $PtSe_2$ and $MoSe_2$.[26] These results confirm the vertically stacked $PtSe_2$/$MoSe_2$ heterojunction. Next, we employed X-ray photoelectron spectroscopy (XPS) to examine the composition of the $PtSe_2$/$MoSe_2$ heterostructures. Based on XPS data (Figure S10), the atomic ratio between Se and Pt/Mo is estimated to be ~1.97, which is very close to the stoichiometry of $MoSe_2$ and $PtSe_2$. More information about the PL spectra and PL and Raman mappings of $PtSe_2$/$MoSe_2$ heterostructures is presented in Figure S11. Note that the weak PL intensity of $PtSe_2$/$MoSe_2$ heterostructures probably results from the charge transfer between $PtSe_2$ and $MoSe_2$.

ADF-STEM was used to investigate the atomic structure of $PtSe_2$/$MoSe_2$ heterostructures. Figure 2a shows the atomic-resolution ADF-STEM image of $PtSe_2$/$MoSe_2$. The periodic Moiré patterns can be clearly observed along the basal plane of the heterostructure, which is caused by the interference from the lattice of monolayer $PtSe_2$ and $MoSe_2$. The fast Fourier transformation (FFT) of the $PtSe_2$/$MoSe_2$ is shown in the inset of Figure 2a. Two different sets of diffraction patterns close to each other were identified. The lattice constants of ~0.38 nm and ~0.33 nm correspond to $PtSe_2$ and $MoSe_2$ respective lattices, indicating the as-synthesized $PtSe_2$ and $MoSe_2$ are single crystals. This is further confirmed by the selected area electron diffraction pattern collected on a much larger region of $PtSe_2$/$MoSe_2$ (over ~5 μm in size), as shown in Figure S12, which only displays one set of diffraction pattern of $PtSe_2$ and $MoSe_2$, respectively. Moreover, the two monolayer lattices are well aligned with each other, which is a strong evidence of the vertically epitaxial growth. The FFT (inset in Figure 2a) does not show the superlattice periodicity, which is expected near the central bright spot, presumably due to its weak signal. However, the periodicity of the Moiré pattern can be directly measured in the atomically resolved image by filtering out the lattice of $PtSe_2$ and $MoSe_2$ (see Figure S13 for more details), which is estimated to be ~2.60 nm. Such a large supercell indicates the highly epitaxial feature as a result of the coupling growth between the two materials. Figure 2b,c shows the inverse FFT images of Figure 2a, which distinguishes the atomic structures of the 1T and 1H phases in $PtSe_2$ and $MoSe_2$, respectively.

Figure 2d shows a low magnification ADF-STEM image of the lateral boundary in the $PtSe_2$/$MoSe_2$ heterostructure. The optical image of a similar structure is shown in Figure S14. The

DOI: 10.1021/acsnano.8b09479
ACS Nano 2019, 13, 10929−10938

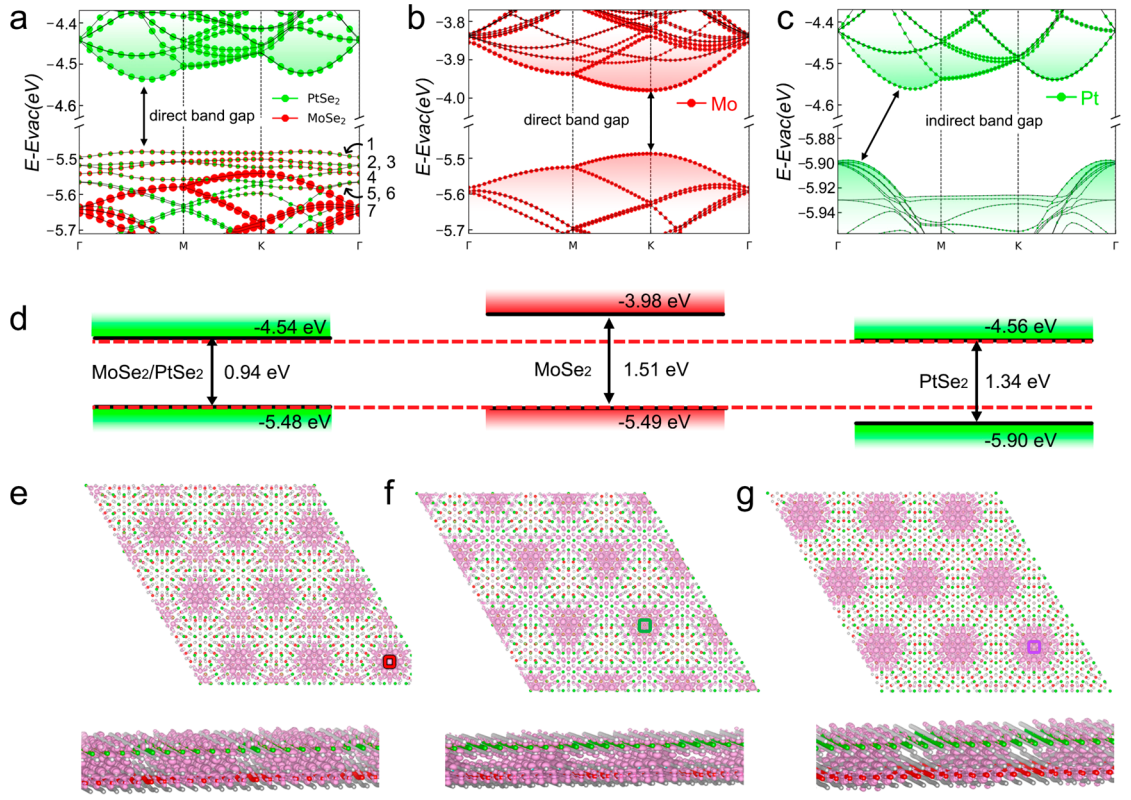

Figure 4. Band alignment and Spatial structures of wave functions for $PtSe_2$(1T)/$MoSe_2$(1H) vertical heterostructures. (a) The band structure of $PtSe_2$(1T)/$MoSe_2$(1H) vertical heterostructure as well as projected contributions of the marked systems. (b and c) Band structures and projected contributions of the marked atoms of deformed monolayer $MoSe_2$ and $PtSe_2$ whose geometry structures are extracted from the relaxed heterostructure. (d) Band alignment of original monolayer $MoSe_2$ and $PtSe_2$ and relaxed $PtSe_2$(1T)/$MoSe_2$(1H) vertical heterostructure. All energies here take the vacuum level as a reference. (e–g) Top and side views of the spatial distribution of modular squared wave functions for the marked bands 1, 4, and 7 in (a), separately. The violet, green, and red rectangles correspond to those in Figure 3. Side views display clearly each type of atom contribution to a certain band.

underneath $MoSe_2$ layer is continuous, thus such structure can be considered as a grain boundary between $PtSe_2$ and $MoSe_2$ monolayers on the $MoSe_2$ substrate. Figure 2e,f shows atomically resolved images of two different regions along the lateral boundaries. In fact, because of the lattice mismatch between $MoSe_2$ and $PtSe_2$, the formation energy of an atomic sharp interface should be very high. Figure 2e shows the initial stage of the lateral boundary, displaying a sharp change from $PtSe_2$ to $MoSe_2$ lattice with some tiny regions of bright contrast along the edge. This indicates that both $PtSe_2$ and $MoSe_2$ lattices have a sharp edge termination without any chemical bonding. Figure 2f shows another region of the lateral boundary away from Figure 2e, where the transition region between the $PtSe_2$/$MoSe_2$ Moiré pattern and bilayer $MoSe_2$ shows an enhanced contrast. This is due to the overlap of the edge regions from the two monolayers, that is, the $PtSe_2$ layer has rolled on top of the bilayer $MoSe_2$ edge, forming a thicker layer which exhibits brighter contrast, as illustrated by the corresponding atomic model (Figure 2g,h). The overlapping region varies and becomes wider (Figure 2d) along the boundary, confirming the overlapping feature in the lateral boundary. This is consistent with our expectation that the $PtSe_2$ is more likely to climb over the $MoSe_2$ edge (second layer $MoSe_2$) during the growth to form a vertically overlapping boundary since the formation energy of an interconnected in-plane boundary is very high, due to their lattice mismatch.

It is known that the interlayer interaction offers great opportunity to study different properties in van der Waals (vdW) solids, for instance, the electronic structure from the Moiré pattern in a vdW heterostructure.[27−29] Substantial research efforts have been devoted to weak interlayer coupled TMDs and their heterostructures, for example, $MoSe_2$ and WSe_2.[27] Strong interlayer coupled two-dimensional (2D) materials have recently been visited,[2,5,30,31] and $PtSe_2$ is a representative among them. An interesting question then arises regarding the interlayer coupling of a heterostructure whose components provide strong and weak interlayer couplings, respectively. The $PtSe_2$/$MoSe_2$ heterostructure synthesized in this work offers an ideal platform for studying this special interlayer interaction. The fully relaxed atomic structure of the $PtSe_2$(1T)/$MoSe_2$(1H) vertical heterostructure is shown in Figure 3. According to the STEM measured Moiré periodicity (Figure 2), a 7 × 7 supercell of the $PtSe_2$ monolayer stacking over an 8 × 8 supercell the $MoSe_2$ monolayer is adopted for modeling the heterostructure. The optimized lattice constant of the supercell is 2.64 nm, only 1.4% larger than the experimental value of 2.60 nm. It is exceptional that $MoSe_2$ appears rumpling in the relaxed heterojunction, suggesting significant interlayer attraction (0.25 eV/$PtSe_2$) between the two layers and stronger bending strength of $PtSe_2$ than that of $MoSe_2$. The interlayer distance d varies from 3.15 to 3.64 Å, whose lower limit is much larger than that of $PtSe_2$ bilayers of 2.55 Å[5] but slightly smaller than that of $MoSe_2$ bilayers of 3.20 Å,[32] implying the interlayer interaction might be stronger than

DOI: 10.1021/acsnano.8b09479
ACS Nano 2019, 13, 10929−10938

that in $MoSe_2$. The mismatched lattices of 1L $PtSe_2$ (3.71 Å for theory and 3.76 Å for experiment) and 1L $MoSe_2$ (3.30 Å for theory and 3.32 Å for experiment) lead to continuously varied stacking orders. There are seven local stacking orders along the supercell lattice. Among them, we found three high-symmetry ones, namely $Se_{inter\text{-}PtSe_2}$ on top of $Se_{inter\text{-}MoSe_2}$ (Figure 3c, denoted by the violet rectangle), Pt on top of $Se_{inter\text{-}MoSe_2}$ (Figure 3d, denoted by the green rectangle), and $Se_{inter\text{-}PtSe_2}$ on top of Mo (Figure 3e, denoted by the red rectangle). The vertical distances of these three stacking orders are 3.64, 3.17, and 3.15 Å, respectively (Figure S15a). Correspondingly, the spatial modulations of local bandgap and valence band maximum (VBM) of this vertical heterostructure are shown in Figures S15b, S16, and S17, respectively, where the variations of bandgaps and VBMs share the same modulation pattern with that of vertical interlayer distances. The Moiré potential (VBM) for the above three high-symmetry stacking orders are −65, −5, and 0 meV, respectively.

Atom-decomposed band structures (Figure 4a) explicitly show seven emerging states (denoted bands 1−7) in addition to a type II band alignment of the heterojunctions. The valence and conduction bands are comprised of the VB of $MoSe_2$ (Mo-d orbital, Se-p orbital) and CB of $PtSe_2$ (Pt-d orbital, Se-p orbital), respectively (Figure 4b,c). Figure 4d illustrates the band alignment before and after forming the heterojunction. The junction has a direct bandgap of 0.94 eV (0.92 eV, w/SOC), reduced from a 1.51 eV (1.39 eV, w/SOC) direct bandgap of $MoSe_2$ and a 1.34 eV (1.19 eV, w/SOC) indirect bandgap of $PtSe_2$, which are in good accordance with their experimental values,that is, 1.55 eV for $MoSe_2$[33] and 1.13 eV for $PtSe_2$.[5] These seven bands are not induced by the aforementioned substantial structural deformation of $MoSe_2$ or $PtSe_2$, as Figure 4b,c shows that the deformation does not change the shape of band structures. They are also not the case of quantum confined states[29] since both $MoSe_2$ and $PtSe_2$ contribute to them. Bands 1−7 are thus regarded as electronically hybridized interfacial states, which result from the frustrated strong-weak interlayer coupling between $PtSe_2$ and $MoSe_2$ layers. These hybridized interfacial states, emerging within the original bandgap of vdW heterojunctions, are of particular interest. Figure 4e−g plots the spatial distributions of the wave function norms of bands 1 (e), 4 (f) and 7 (g). They are located around the aforementioned three particular stacking positions as marked by red, green, and violet rectangles, respectively, indicating each interfacial state corresponds to one stacking configuration. The side views (Figure 4e−g) suggest that these interfacial states are comprised of p_z orbitals of the interfacial Se layer of $MoSe_2$ and both Se layers of $PtSe_2$ and d_{z^2} orbital of Pt and Mo atoms, implying that the outer Se layer of $MoSe_2$ is not involved in forming these interfacial states. These wave functions are more localized than those of VB and CB (Figure S18) in real-space, consistent with the flat band dispersion in the *k*-space. These spatially localized bands suggest that electron−hole pairs of a given energy are excited at a certain stacking position, as marked in Figure 3a. The $PtSe_2$ involved in forming these bands may lead to inter- and intralayer mixed excitation mechanisms for the interlayer excitons, which should be interesting for further exploration. In the light of these, interfacial states are of particular interest in terms of exciton dynamics in the heterojunction.

As discussed above, STEM images and first-principles calculations have demonstrated the vertical stacking and emerging interfacial states in $PtSe_2/MoSe_2$ heterostructure due to the frustrated strong−weak interlayer coupling between $PtSe_2$ and $MoSe_2$ layers. In order to further elucidate the interfacial states and the interlayer coupling, we conducted the electrostatic force microscopy (EFM) to study the charge distribution in $PtSe_2/MoSe_2$ heterostructures. EFM has been proven as an effective method to evaluate the local electrical properties of 2D materials.[34,35] The optical image and topography of $PtSe_2/MoSe_2$ heterostructure are shown in Figure 5a,c, respectively. The corresponding AFM image is

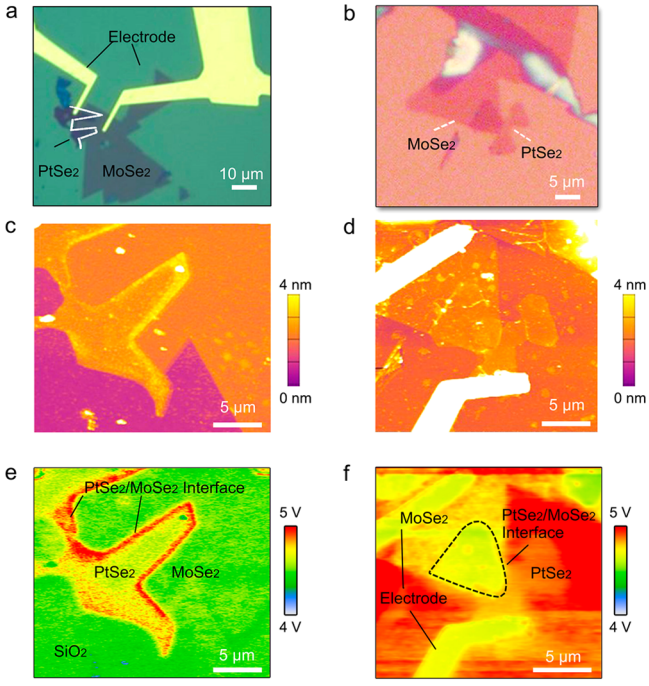

Figure 5. EFM measurements. (a and c) Optical image and height topography of $PtSe_2/MoSe_2$ heterostructure grown by one-step CVD. (b and d) Optical image and topography of transferred $PtSe_2/MoSe_2$ heterostructure. (e) EFM image of $PtSe_2/MoSe_2$, identifying the edge state at the edge of $PtSe_2$. (f) EFM image of transferred $PtSe_2/MoSe_2$ under zero bias voltage, indicating a semiconducting behavior of $PtSe_2$ and $MoSe_2$.

presented in Figure S19. The EFM image of the heterostructure shown in Figure 5e indicates that strong charge accumulation takes place on the edge of $PtSe_2$, which is attributed to the charge transfer from uncovered monolayer $MoSe_2$ to $PtSe_2/MoSe_2$ heterostructure induced by the slightly lowered VB of $PtSe_2$ and lifted CB of $MoSe_2$. For comparison, EFM measurement was carried out on a transferred $PtSe_2/MoSe_2$ heterostructure. The optical image, topography, and EFM image are shown in Figure 5b,d,f, respectively. The absence of edge states clearly illustrates that the strong interlayer coupling is not formed in the transferred heterostructure. These results demonstrate the strong interlayer coupling between strong interlayer-coupled $PtSe_2$ and weak interlayer-coupled $MoSe_2$, which agrees well with the results of electronically hybridized interface states from first-principles calculations.

The type II band alignment offers the possibility to study the charge transfer induced by the interlayer coupling in $PtSe_2/$

DOI: 10.1021/acsnano.8b09479
ACS Nano 2019, 13, 10929−10938

$MoSe_2$ heterostructure. We further studied the charge transfer kinetics of $PtSe_2/MoSe_2$ heterostructure through ultrafast transient dynamics measurement. The ultrafast transient reflection dynamics of the heterostructure along with the $PtSe_2$ and $MoSe_2$ monolayers (optical images are shown as insets in Figure 6a,b) were measured using 910 nm pump

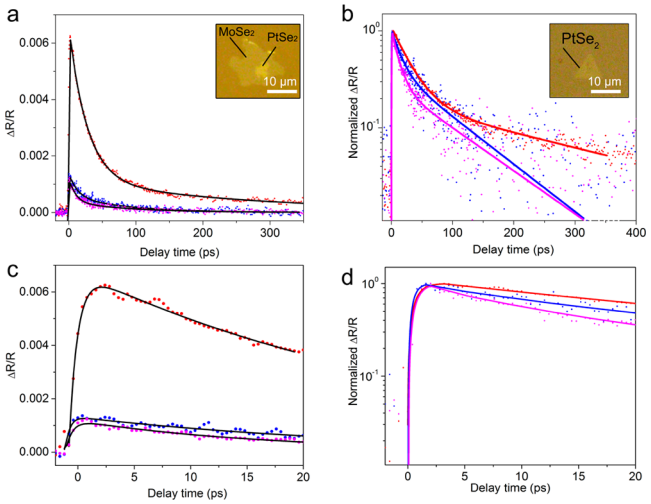

Figure 6. Ultrafast electron dynamics of $MoSe_2$, $PtSe_2$, and $PtSe_2/MoSe_2$ heterostructure. (a) Differential reflection kinetics of $PtSe_2/MoSe_2$ heterostructure (red), $PtSe_2$ (blue), and $MoSe_2$ (pink) monolayers excited at 910 nm and probed at 780 nm with the pump and probe power around 100 and 70 μW, respectively. Insets is the optical image of $PtSe_2/MoSe_2$ heterostructure. The kinetics at shorter time scale is shown in (c). (b) Comparison of the normalized differential reflection kinetics of the heterostructure and monolayers. Inset is the optical image of $PtSe_2$. The corresponding kinetics at shorter time scale of $PtSe_2$ is displayed in (d).

excitation and 780 nm probe with pump and probe powers of 100 and 70 μW, respectively. According to the reported experimental band gaps of monolayer $MoSe_2$ (1.55 eV)[33] and $PtSe_2$ (1.13 eV)[5] as well as our band calculation results, the 910 nm pump excitation will only excite carriers in $PtSe_2$, since the photon energy is below the bandgap of $MoSe_2$. Thus, direct one-photon absorption of 910 nm wavelength will not occur in $MoSe_2$ layers. As shown in Figure 6, the transient response from the heterostructure is very different from that of monolayers under the same pump–probe power. First, the transient response amplitude of the heterostructure is ~3 times higher than that of individual monolayers (Figure 6a). Second, the initial rising time of the transient response is slightly slower in heterostructure than that in individual monolayers. Third, the subsequent decay dynamics are relatively longer for heterostructure than either $PtSe_2$ or $MoSe_2$ monolayer alone. The latter two features can be clearly visualized from the normalized transient reflection kinetics shown in Figure 6b.

Compared with monolayer $PtSe_2$, the relatively slow rising kinetics of the $PtSe_2/MoSe_2$ heterostructure proves the hole transfer between $PtSe_2$ and $MoSe_2$. More specifically, the pump (910 nm) excites electrons from the VB to the CB of $PtSe_2$ through one photon absorption, along with a rapid hole transfer from $PtSe_2$ to $MoSe_2$ layer due to their type II band alignment. The rising time (τ_r) of the heterostructure kinetics, which describes the hole transfer between $PtSe_2$ and $MoSe_2$, is found to be 0.5–0.9 ps. This value is longer than that of $PtSe_2$ monolayers and consistent with the previous reports on the charge-transfer process in heterostructures.[36] As a result of the hole transfer from $PtSe_2$ to $MoSe_2$, the probe reflection is modified due to the hole occupation in $MoSe_2$ and contributes to transient reflection signal of the 780 nm probe. The magnitude of peak transient signal is also 5 times larger than that in individual $PtSe_2$ or $MoSe_2$ monolayers.

The following decay kinetics after the maximum transient reflection of the heterostructure and monolayers can be fitted with biexponential function $I(t) = A \times \exp(-t/\tau_{d1}) + B \times \exp(-t/\tau_{d2})$, where τ_{d1} and τ_{d2} represent the fast and slow decay time constants, respectively. The fast (τ_{d1} = 27.5 ± 0.3 ps) and slow (τ_{d2} = 280.1 ± 12.3 ps) decay time constants of the heterostructure are nearly 2–3 times larger than decay time constants of individual $PtSe_2$ (τ_{d1} = 14.9 ± 1.8 ps, τ_{d2} = 88.8 ± 9 ps) and $MoSe_2$ (τ_{d1} = 11.7 ± 0.9 ps, τ_{d2} = 97.9 ± 9 ps) monolayers. The decay time of $PtSe_2/MoSe_2$ heterostructure is much longer than that of $PtSe_2$ and $MoSe_2$ monolayers, which suggests an efficient separation of the electron–hole in $PtSe_2/MoSe_2$ heterostructures.

CONCLUSIONS

In summary, we have successfully synthesized $PtSe_2/MoSe_2$ vertically stacked heterojunctions *via* a one-step CVD method. STEM results confirm the formation of vertical and lateral heterostructures between strong interlayer-coupled $PtSe_2$ and weak interlayer-coupled $MoSe_2$. First-principle calculations confirm a direct band gap structure and type II band alignment between $PtSe_2$ and $MoSe_2$. The emerging electronically hybridized interface states within the original bandgap are the observed in CVD-grown 2D TMD heterostructures, which have been confirmed by the edge states unveiled by EFM. Ultrafast electron dynamics measurements suggest that the holes transfer from $MoSe_2$ to $PtSe_2$, confirming the theoretically predicted band alignment and strong interlayer coupling between $PtSe_2$ and $MoSe_2$. This strategy shows the way toward the synthesis of heterostructures based on group 10 TMDs, and our results show great potential of $PtSe_2/MoSe_2$ heterostructures for applications in electronic and optoelectronic devices.

METHODS

$PtSe_2$ and $PtSe_2/MoSe_2$ Growth. In our experiment, $PtCl_2$, MoO_3, and Se were used as sources (all reactants were bought from Alfa Aesar with purity more than 99%). The polycrystalline $PtSe_2$ film was grown in a quartz tube (1 in. diameter, 36 cm length) at 400 °C. Single $PtSe_2$ and $PtSe_2/MoSe_2$ flakes were synthesized using the same setup at 810 °C. The distance between $PtCl_2$ and mixed powder is ~5 mm. H_2/Ar was used as the carrier gas. Specifically, the alumina boat (8 cm × 1.1 cm × 1.2 cm) containing Mo and Pt precursors was put in the middle of the quartz tube. The distance between the precursors and substrate is around 1.2 cm. For $PtSe_2$, Ar (or Ar/H_2 mix) gas with a flow rate of 80 (80/10) sccm was used as the carrier gas, and the Al_2O_3 boat containing 10 mg $PtCl_2$ was put in the center of the tube. The SiO_2/Si substrate was placed on the boat with surface downside. Another Al_2O_3 boat containing 100 mg Se powder was put in the upstream zone. The temperature was ramped up to 810 °C in 16 min and kept at the reaction temperature for 15 min. Then the furnace was cooled down to room temperature naturally.

For $PtSe_2/MoSe_2$, the Ar/H_2 mixed gas with a flow rate of 80/10 sccm was used as the carrier gas, and the Al_2O_3 boat containing 5 mg $PtCl_2$ and 5 mg (4 mg MoO_3 and 1 mg NaCl) was put in the center of the tube. The distance between $PtCl_2$ and MoO_3/NaCl was 5 mm. SiO_2/Si or sapphire substrate was placed on the boat with surface downside. Another Al_2O_3 boat containing 10 g Se powder was put on

DOI: 10.1021/acsnano.8b09479
ACS Nano 2019, 13, 10929–10938

the upstream zone. The temperature was ramped up to 810 °C in 16 min and kept at the reaction temperature for 10 min. The furnace was then cooled down to room temperature gradually.

For $PtSe_2/MoSe_2$ heterostructure prepared by mechanic exfoliation and transfer, a 0.8 μm layer of poly(methyl methacrylate) (PMMA) was spin-coated on the $MoSe_2$ wafer and then baked at 180 °C for 4 min. Afterward, the wafer was immersed in KOH solution (1M) to etch the SiO_2 layer. After lift-off, the $PMMA/PtSe_2/MoSe_2$ film was transferred into DI water for several cycles to wash away the residual contaminants and then dried in air. Next, PMMA with $MoSe_2$ samples were transferred on $PtSe_2$ flakes. Last, the wafer was immersed in acetone solution to resolve the PMMA.

Raman Characterization. Raman measurements with an excitation laser of 532 nm were performed using WITEC alpha 300R Confocal Raman system. Before Raman characterization, the system was calibrated with the Raman peak of Si at 520 cm^{-1}. The laser powers were set at <1 mW to avoid overheat the samples.

AFM. AFM measurement was carried out using the Asylum Research, Cypher S system with a cantilever tip of Arrow-NCR-50-Silicon SPM-Sensor (coating on detector sider: Al-coating). The force constant is 42 N/m.

XPS Characterization. XPS measurement was performed using a monochromated Al Kα source ($h\nu$ = 1486.6 eV) and a 128 channel mode detection PHI original detector. XPS spectra were acquired at a pass energy of 140 eV and takeoff angle of 45°.

TEM and STEM Characterization. The STEM samples were prepared with a PMMA assisted method. A layer of PMMA about 0.8 μm in thickness was spin-coated on the wafer with samples deposited and then baked at 140 °C for 5 min. Afterward, the wafer was immersed in KOH solution (1 M) to etch the SiO_2 layer overnight. After lift-off, the $PMMA/PtSe_2/MoSe_2$ film was transferred into DI water for several cycles to wash away the residual contaminants and then fished by a TEM grid (Quantifoil Mo grid). The transferred specimen was dried naturally in ambient environment and then dropped into acetone overnight to wash away the PMMA coating layers. The STEM imaging was done in a JEOL 2100F with delta probe corrector, which corrects the aberration up to fifth order, resulting in a probe size of 1.2 Å. The imaging was conducted at an acceleration voltage of 60 kV. The convergent angle for illumination is about 35 mrad, with a collection detector angle ranging from 45 to 200 mrad. The BF-TEM and diffraction imaging was conducted in a FEI Tecnai F30 microscope operating at 80 kV. All imaging was performed at room temperature.

Ultrafast Transient Reflection Spectroscopy. An infrared optical parametric amplifier (OPA) pumped by a 60 fs, 250 kHz Ti:Sapphire regenerative amplifier (RegA) was used in the transient reflection measurements. The idler from OPA at 1840 nm used as pump is frequency doubled to 920 nm (~180 fs). The 780 nm component filtered from white light supercontinuum, which is generated from a sapphire crystal pumped with compressed remnant 800 nm beam of OPA, was used as a probe. Both pump and probe pulses were linearly polarized. A 40× reflective objective lens was used to focus the co-propagating pump probe spots onto the sample. The reflected probe was collected by the same objective lens and routed through a monochromator followed by a photodetector. The detected probe reflection was read by a lock-in amplifier referenced to a mechanically chopped pump. The probe spot size was estimated to be 2 μm. The pump photon fluency was estimated to be around 1×10^{16} photons/cm^2.

Calculations. Density functional theory (DFT) calculations were performed using the generalized gradient approximation for the exchange−correlation potential, the projector augmented wave method,[37,38] and a plane-wave basis set as implemented in the Vienna *ab initio* simulation package (VASP).[39] For the configuration of $PtSe_2(1T)/MoSe_2(1H)$ vertical heterostructure, a (7×7) supercell is adopted for $PtSe_2(1T)$, while a (8×8) supercell for $MoSe_2(1H)$ and a vacuum layer of 25 Å in thickness between periodic images was employed. The energy cutoff for the plane-wave basis was set to 500 eV for all calculations except those with spin−orbit coupling (SOC) into consideration where an energy cutoff of 300 eV is utilized. The inclusion of SOC has little influence on the shape of the band structures but induces appreciable band energy shifts or band splitting, for example, a separation of 30−50 meV for the emerging hybridized interfacial states marked with bands 1−7 in Figure 4a. All calculations and analysis shown in Figure 4a−c were performed in the same supercell which consisted of a (7×7) supercell of $PtSe_2(1T)$ and a (8×8) supercell of $MoSe_2(1H)$. In optimizing the system geometry, vdW interactions were considered at the vdW-DF[40] level with the optB86b (optB86b-vdW) functional for exchange potential,[41] which was recently demonstrated more accurate in describing structural properties of layered materials than other functionals.[30,31,42,43] All atoms in the supercell were allowed to relax until the residual force per atom was <0.02 eV·$Å^{-1}$.

ASSOCIATED CONTENT

Supporting Information

The Supporting Information is available free of charge on the ACS Publications website at DOI: 10.1021/acsnano.8b09479.

Further experimental and theoretical details, including different size of vertical heterostructures, thickness and Raman spectrum of $PtSe_2$, optical images of $PtSe_2/MoSe_2$ heterostructure, growth of $PtSe_2$ on exfoliated $MoSe_2$ flakes, optical image and TEM characterization of polycrystalline $PtSe_2$, optical images, AFM images and Raman spectra of $PtSe_2$ single crystals, optical images and AFM images of $PtSe_2$ single crystals synthesized on sapphire substrate, XPS characterizations of $PtSe_2/MoSe_2$ heterostructure, PL spectra, PL and Raman mappings of $PtSe_2/MoSe_2$ with different shape, SEAD patterns of $PtSe_2/MoSe_2$ heterostructure, large-scale STEM image of vertically stacked $PtSe_2/MoSe_2$ heterostructure, optical image of in plane and vertical $PtSe_2/MoSe_2$ heterostructures, spatial distribution of interlayer distance and bandgap for $PtSe_2(1T)/MoSe_2(1H)$ vertical heterostructure, spatial distribution of bandgap for $PtSe_2(1T)/MoSe_2(1H)$ vertical heterostructure, spatial distribution of VBM for $PtSe_2(1T)/MoSe_2(1H)$ vertical heterostructure, spatial structures of wave functions for $PtSe_2(1T)/MoSe_2(1H)$ vertical heterostructures, AFM image and thickness of $PtSe_2$ on $MoSe_2$ (PDF)

AUTHOR INFORMATION

Corresponding Authors

*E-mail: z.liu@ntu.edu.sg.
*E-mail: wji@ruc.edu.cn.
*E-mail: sundong@pku.edu.cn.
*E-mail: lin.junhao.stem@gmail.com.

ORCID

Xianghua Kong: 0000-0003-4381-4955
Zhihai Cheng: 0000-0003-4938-4490
Ting Yu: 0000-0001-5782-1588
Kazu Suenaga: 0000-0002-6107-1123
Dong Sun: 0000-0002-0898-4548
Wei Ji: 0000-0001-5249-6624
Zheng Liu: 0000-0002-8825-7198

Author Contributions

●These authors contributed equally to this work.

Notes

The authors declare no competing financial interest.

DOI: 10.1021/acsnano.8b09479
ACS Nano 2019, 13, 10929−10938

ACKNOWLEDGMENTS

This work is supported by the Singapore National Research Foundation under NRF RF award no. NRF-RF2013-08. MOE Tier 1 RG7/18, MOE Tier 2 MOE2015-T2-2-007, MOE2016-T2-2-153, MOE2017-T2-2-136, MOE Tier 3 MOE2018-T3-1-002, and A*Star QTE program. J.L. and K.S. acknowledge JST-ACCEL and JSPS KAKENHI (JP16H06333 and P16823) for financial support. This work was also supported by the Pico Center at MCPC of SUSTech that receives support from Presidential fund and Development and Reform Commission of Shenzhen Municipality. Z.H.C. and W.J. thank the Ministry of Science and Technology (MOST) of China (no. 2016YFA0200700, no. 2018YFE0202700) for financial support. X.K. Z.H.C., R.X., and W.J. were supported by the National Natural Science Foundation of China (grant nos. 11274380, 91433103, 11622437, 21622304, 61674045, 11604063, 11974422, and 61674171), the Fundamental Research Funds for the Central Universities of China and the Research Funds of Renmin University of China (grant nos. 16XNLQ01 and 18XNLG01), and the Strategic Priority Research Program of Chinese Academy of Sciences (grant no. XDB30000000). This research is partially supported by the Science, Technology, and Innovation Commission of Shenzhen Municipality (no. ZDSYS20170303165926217). X.K. thanks Prof. Hong Guo at McGill University for financial support. C.M., W.L., and D.S. were supported by the National Natural Science Foundation of China (grant nos. 11674013, 91750109). Calculations were performed at the physics lab of high-performance computing of Renmin University of China, Shanghai Supercomputer Center, McGill University, Calcul Québec, and Compute Canada.

REFERENCES

(1) Yao, W.; Wang, E. Y.; Huang, H. Q.; Deng, K.; Yan, M. Z.; Zhang, K. N.; Miyamoto, K.; Okuda, T.; Li, L. F.; Wang, Y. L.; Gao, H. J.; Liu, C. X.; Duan, W. H.; Zhou, S. Y. Direct Observation of Spin-Layer Locking by Local Rashba Effect in Monolayer Semiconducting $PtSe_2$ Film. *Nat. Commun.* **2017**, *8*, 142216.

(2) Zhao, Y. D.; Qiao, J. S.; Yu, P.; Hu, Z. X.; Lin, Z. Y.; Lau, S. P.; Liu, Z.; Ji, W.; Chai, Y. Extraordinarily Strong Interlayer Interaction in 2D Layered PtS_2. *Adv. Mater.* **2016**, *28*, 2399−2407.

(3) Ciarrocchi, A.; Avsar, A.; Ovchinnikov, D.; Kis, A. Thickness-Modulated Metal-to-Semiconductor Transformation in a Transition Metal Dichalcogenide. *Nat. Commun.* **2018**, *9*, 919.

(4) Li, P. F.; Li, L.; Zeng, X. C. Tuning the Electronic Properties of Monolayer and Bilayer $PtSe_2$ *via* Strain Engineering. *J. Mater. Chem. C* **2016**, *4*, 3106−3112.

(5) Zhao, Y. D.; Qiao, J. S.; Yu, Z. H.; Yu, P.; Xu, K.; Lau, S. P.; Zhou, W.; Liu, Z.; Wang, X. R.; Ji, W.; Chai, Y. High-Electron-Mobility and Air-Stable 2D Layered $PtSe_2$ FETs. *Adv. Mater.* **2017**, *29*, 1604230.

(6) Zeng, L.; Lin, S.; Lou, Z.; Yuan, H.; Long, H.; Li, Y.; Lu, W.; Lau, S. P.; Wu, D.; Tsang, Y. H. Ultrafast and Sensitive Photodetector Based on a $PtSe_2$/Silicon Nanowire Array Heterojunction with a Multiband Spectral Response from 200 to 1550 nm. *NPG Asia Mater.* **2018**, *10*, 352−362.

(7) Yu, X. C.; Yu, P.; Wu, D.; Singh, B.; Zeng, Q. S.; Lin, H.; Zhou, W.; Lin, J. H.; Suenaga, K.; Liu, Z.; Wang, Q. J. Atomically Thin Noble Metal Dichalcogenide: A Broadband Mid-Infrared Semiconductor. *Nat. Commun.* **2018**, *9*, 1545.

(8) Chia, X. Y.; Adriano, A.; Lazar, P.; Sofer, Z.; Luxa, J.; Pumera, M. Layered Platinum Dichalcogenides (PtS_2, $PtSe_2$, and $PtTe_2$) Electrocatalysis: Monotonic Dependence on the Chalcogen Size. *Adv. Funct. Mater.* **2016**, *26*, 4306−4318.

(9) Yim, C.; Lee, K.; McEvoy, N.; O'Brien, M.; Riazimehr, S.; Berner, N. C.; Cullen, C. P.; Kotakoski, J.; Meyer, J. C.; Lemme, M. C.; Duesberg, G. S. High-Performance Hybrid Electronic Devices from Layered $PtSe_2$ Films Grown at Low Temperature. *ACS Nano* **2016**, *10*, 9550−9558.

(10) Liu, K.; Zheng, B. J.; Wu, J. J.; Chen, Y. F.; Wang, X. Q.; Qi, F.; He, D. W.; Zhang, W. L.; Li, Y. R. Synthesis of Two-Dimensional Semiconductor Single-Crystal $PtSe_2$ under High Pressure. *J. Mater. Sci.* **2018**, *53*, 1256−1263.

(11) Yan, M. Z.; Wang, E. Y.; Zhou, X.; Zhang, G. Q.; Zhang, H. Y.; Zhang, K. N.; Yao, W.; Lu, N. P.; Yang, S. Z.; Wu, S. L.; Yoshikawa, T.; Miyamoto, K.; Okuda, T.; Wu, Y.; Yu, P.; Duan, W. H.; Zhou, S. Y. High Quality Atomically Thin $PtSe_2$ Films Grown by Molecular Beam Epitaxy. *2D Mater.* **2017**, *4*, 045015.

(12) Wang, Y. L.; Li, L. F.; Yao, W.; Song, S. R.; Sun, J. T.; Pan, J. B.; Ren, X.; Li, C.; Okunishi, E.; Wang, Y. Q.; Wang, E. Y.; Shao, Y.; Zhang, Y. Y.; Yang, H. T.; Schwier, E. F.; Iwasawa, H.; Shimada, K.; Taniguchi, M.; Cheng, Z. H.; Zhou, S. Y.; et al. Monolayer $PtSe_2$, a New Semiconducting Transition-Metal-Dichalcogenide, Epitaxially Grown by Direct Selenization of Pt. *Nano Lett.* **2015**, *15*, 4013−4018.

(13) Wang, Z. G.; Li, Q.; Besenbacher, F.; Dong, M. D. Facile Synthesis of Single Crystal $PtSe_2$ Nanosheets for Nanoscale Electronics. *Adv. Mater.* **2016**, *28*, 10224−10229.

(14) Zhou, J. D.; Lin, J. H.; Huang, X. W.; Zhou, Y.; Chen, Y.; Xia, J.; Wang, H.; Xie, Y.; Yu, H. M.; Lei, J. C.; Wu, D.; Liu, F. C.; Fu, Q. D.; Zeng, Q. S.; Hsu, C. H.; Yang, C. L.; Lu, L.; Yu, T.; Shen, Z. X.; Lin, H.; et al. A Library of Atomically Thin Metal Chalcogenides. *Nature* **2018**, *556*, 355−359.

(15) Li, M. Y.; Shi, Y. M.; Cheng, C. C.; Lu, L. S.; Lin, Y. C.; Tang, H. L.; Tsai, M. L.; Chu, C. W.; Wei, K. H.; He, J. H.; Chang, W. H.; Suenaga, K.; Li, L. J. Epitaxial Growth of a Monolayer WSe_2-MoS_2 Lateral *p-n* Junction with an Atomically Sharp Interface. *Science* **2015**, *349*, 524−528.

(16) Chen, K.; Wan, X.; Wen, J. X.; Xie, W. G.; Kang, Z. W.; Zeng, X. L.; Chen, H. J.; Xu, J. B. Electronic Properties of MoS_2-WS_2 Heterostructures Synthesized with Two-Step Lateral Epitaxial Strategy. *ACS Nano* **2015**, *9*, 9868−9876.

(17) Chen, K.; Wan, X.; Xie, W. G.; Wen, J. X.; Kang, Z. W.; Zeng, X. L.; Chen, H. J.; Xu, J. B. Lateral Built-in Potential of Monolayer MoS_2-WS_2 in-Plane Heterostructures by a Shortcut Growth Strategy. *Adv. Mater.* **2015**, *27*, 6431−6437.

(18) Li, X. F.; Lin, M. W.; Lin, J. H.; Huang, B.; Puretzky, A. A.; Ma, C.; Wang, K.; Zhou, W.; Pantelides, S. T.; Chi, M. F.; Kravchenko, I.; Fowlkes, J.; Rouleau, C. M.; Geohegan, D. B.; Xiao, K. Two-Dimensional GaSe/$MoSe_2$ Misfit Bilayer Heterojunctions by Van Der Waals Epitaxy. *Sci. Adv.* **2016**, *2*, No. e1501882.

(19) Yoo, Y. D.; Degregorio, Z. P.; Johns, J. E. Seed Crystal Homogeneity Controls Lateral and Vertical Heteroepitaxy of Monolayer MoS_2 and WS_2. *J. Am. Chem. Soc.* **2015**, *137*, 14281−14287.

(20) Zhang, T.; Jiang, B.; Xu, Z.; Mendes, R. G.; Xiao, Y.; Chen, L. F.; Fang, L. W.; Gemming, T.; Chen, S. L.; Rummeli, M. H.; Fu, L. Twinned Growth Behaviour of Two-Dimensional Materials. *Nat. Commun.* **2016**, *7*, 13911.

(21) Gong, Y. J.; Lin, J. H.; Wang, X. L.; Shi, G.; Lei, S. D.; Lin, Z.; Zou, X. L.; Ye, G. L.; Vajtai, R.; Yakobson, B. I.; Terrones, H.; Terrones, M.; Tay, B. K.; Lou, J.; Pantelides, S. T.; Liu, Z.; Zhou, W.; Ajayan, P. M. Vertical and in-Plane Heterostructures from WS_2/MoS_2 Monolayers. *Nat. Mater.* **2014**, *13*, 1135−1142.

(22) Duan, X. D.; Wang, C.; Shaw, J. C.; Cheng, R.; Chen, Y.; Li, H. L.; Wu, X. P.; Tang, Y.; Zhang, Q. L.; Pan, A. L.; Jiang, J. H.; Yu, R. Q.; Huang, Y.; Duan, X. F. Lateral Epitaxial Growth of Two-Dimensional Layered Semiconductor Heterojunctions. *Nat. Nanotechnol.* **2014**, *9*, 1024−1030.

(23) Wang, X. L.; Gong, Y. J.; Shi, G.; Chow, W. L.; Keyshar, K.; Ye, G. L.; Vajtai, R.; Lou, J.; Liu, Z.; Ringe, E.; Tay, B. K.; Ajayan, P. M. Chemical Vapor Deposition Growth of Crystalline Monolayer $MoSe_2$. *ACS Nano* **2014**, *8*, 5125−5131.

DOI: 10.1021/acsnano.8b09479
ACS Nano 2019, 13, 10929−10938

(24) O'Brien, M.; McEvoy, N.; Motta, C.; Zheng, J. Y.; Berner, N. C.; Kotakoski, J.; Elibol, K.; Pennycook, T. J.; Meyer, J. C.; Yim, C.; Abid, M.; Hallam, T.; Donegan, J. F.; Sanvito, S.; Duesberg, G. S. Raman Characterization of Platinum Diselenide Thin Films. *2D Mater.* **2016**, *3*, 021004.
(25) Kim, K.; Lee, J. U.; Nam, D.; Cheong, H. Davydov Splitting and Excitonic Resonance Effects in Raman Spectra of Few-Layer $MoSe_2$. *ACS Nano* **2016**, *10*, 8113−20.
(26) Nam, D.; Lee, J. U.; Cheong, H. Excitation Energy Dependent Raman Spectrum of $MoSe_2$. *Sci. Rep.* **2015**, *5*, 17113.
(27) Zhang, C. D.; Chuu, C. P.; Ren, X. B.; Li, M. Y.; Li, L. J.; Jin, C. H.; Chou, M. Y.; Shih, C. K. Interlayer Couplings, Moire Patterns, and 2D Electronic Superlattices in MoS_2/WSe_2 Hetero-Bilayers. *Sci. Adv.* **2017**, *3*, No. e1601459.
(28) Hong, J. H.; Wang, C.; Liu, H. J.; Ren, X. B. A.; Chen, J. L.; Wang, G. Y.; Jia, J. F.; Xie, M. H.; Jin, C. H.; Ji, W.; Yuan, J.; Zhang, Z. Inversion Domain Boundary Induced Stacking and Bandstructure Diversity in Bilayer $MoSe_2$. *Nano Lett.* **2017**, *17*, 6653−6660.
(29) Pan, Y.; Folsch, S.; Nie, Y. F.; Waters, D.; Lin, Y. C.; Jariwala, B.; Zhang, K. H.; Cho, K.; Robinson, J. A.; Feenstra, R. M. Quantum-Confined Electronic States Arising from the Moire Pattern of MoS_2-WSe_2 Heterobilayers. *Nano Lett.* **2018**, *18*, 1849−1855.
(30) Qiao, J.; Pan, Y.; Yang, F.; Wang, C.; Chai, Y.; Ji, W. Few-Layer Tellurium: One-Dimensional-Like Layered Elementary Semiconductor with Striking Physical Properties. *Sci. Bull.* **2018**, *63*, 159−168.
(31) Qiao, J. S.; Kong, X. H.; Hu, Z. X.; Yang, F.; Ji, W. High-Mobility Transport Anisotropy and Linear Dichroism in Few-Layer Black Phosphorus. *Nat. Commun.* **2014**, *5*, 4475.
(32) Terrones, H.; Lopez-Urias, F.; Terrones, M. Novel Hetero-Layered Materials with Tunable Direct Band Gaps by Sandwiching Different Metal Disulfides and Diselenides. *Sci. Rep.* **2013**, *3*, 1549.
(33) Tongay, S.; Zhou, J.; Ataca, C.; Lo, K.; Matthews, T. S.; Li, J. B.; Grossman, J. C.; Wu, J. Q. Thermally Driven Crossover from Indirect toward Direct Bandgap in 2D Semiconductors: $MoSe_2$ *versus* MoS_2. *Nano Lett.* **2012**, *12*, 5576−5580.
(34) Datta, S. S.; Strachan, D. R.; Mele, E. J.; Johnson, A. T. C. Surface Potentials and Layer Charge Distributions in Few-Layer Graphene Films. *Nano Lett.* **2009**, *9*, 7−11.
(35) Gao, T.; Song, X. J.; Du, H. W.; Nie, Y. F.; Chen, Y. B.; Ji, Q. Q.; Sun, J. Y.; Yang, Y. L.; Zhang, Y. F.; Liu, Z. F. Temperature-Triggered Chemical Switching Growth of in-Plane and Vertically Stacked Graphene-Boron Nitride Heterostructures. *Nat. Commun.* **2015**, *6*, 6835.
(36) Hong, X. P.; Kim, J.; Shi, S. F.; Zhang, Y.; Jin, C. H.; Sun, Y. H.; Tongay, S.; Wu, J. Q.; Zhang, Y. F.; Wang, F. Ultrafast Charge Transfer in Atomically Thin MoS_2/WS_2 Heterostructures. *Nat. Nanotechnol.* **2014**, *9*, 682−686.
(37) Kresse, G.; Joubert, D. From Ultrasoft Pseudopotentials to the Projector Augmented-Wave Method. *Phys. Rev. B: Condens. Matter Mater. Phys.* **1999**, *59*, 1758−1775.
(38) Blochl, P. E. Projector Augmented-Wave Method. *Phys. Rev. B: Condens. Matter Mater. Phys.* **1994**, *50*, 17953−17979.
(39) Monkhorst, H. J.; Pack, J. D. Special Points for Brillouin-Zone Integrations. *Phys. Rev. B* **1976**, *13*, 5188−5192.
(40) Dion, M.; Rydberg, H.; Schroder, E.; Langreth, D. C.; Lundqvist, B. I. Van Der Waals Density Functional for General Geometries. *Phys. Rev. Lett.* **2004**, *92*, 246401.
(41) Klimes, J.; Bowler, D. R.; Michaelides, A. Van Der Waals Density Functionals Applied to Solids. *Phys. Rev. B: Condens. Matter Mater. Phys.* **2011**, *83*, 195131.
(42) Hu, Z. X.; Lan, H. P.; Ji, W. Role of the Dispersion Force in Modeling the Interfacial Properties of Molecule-Metal Interfaces: Adsorption of Thiophene on Copper Surfaces. *Sci. Rep.* **2015**, *4*, 5036.
(43) Wu, J. B.; Hu, Z. X.; Zhang, X.; Han, W. P.; Lu, Y.; Shi, W.; Qiao, X. F.; Ijias, M.; Milana, S.; Ji, W.; Ferrari, A. C.; Tan, P. H. Interface Coupling in Twisted Multilayer Graphene by Resonant Raman Spectroscopy of Layer Breathing Modes. *ACS Nano* **2015**, *9*, 7440−7449.

DOI: 10.1021/acsnano.8b09479
ACS Nano 2019, 13, 10929−10938